Biophysical Journal, Volume *114*

Supplemental Information

Effect of Loading History on Airway Smooth Muscle Cell-Matrix Adhesions

Linda Irons, Markus R. Owen, Reuben D. O'Dea, and Bindi S. Brook

Effect of loading history on airway smooth muscle cell–matrix adhesions: Supporting material

Linda Irons, Markus R. Owen, Reuben D. O'Dea, Bindi S. Brook
Centre for Mathematical Medicine and Biology, School of Mathematical Sciences
University of Nottingham, Nottingham, NG7 2RD, UK

Here we present further details about the numerical simulation of the discrete and continuum models (Section S.1), a list of the parameter values used (Section S.2), and additional figures to support and extend the continuum model results in Section 3 of the main text (Section S.3).

S.1 Numerical methods

Both models were implemented in MATLAB 2016b, as detailed below.

S.1.1 Discrete simulations

The algorithm employed in the discrete stochastic–elastic simulations (see Section 2.1) is summarised as follows. We employ a first reaction method [1] to select the stochastic binding and unbinding reactions.

Algorithm S1 Discrete stochastic–elastic model

1: Initialise actin and ECM spring networks and relax to mechanical equilibrium.
2: **while** $\hat{t} < \hat{T}$ **do**
3: Calculate binding and unbinding propensities, a_i, based on pairwise distances (where $i \in [1, ...N]$ and N denotes the number of possible reactions).
4: Generate a uniformly distributed random number, r_1, from the interval $(0, 1)$, to calculate the time elapsed before the next reaction, $\hat{\tau} = \frac{1}{a_0}\ln(1/r_1)$. The constant a_0 is the sum of all reaction propensities, $a_0 = \sum_{i=1}^{N} a_i$.
5: **if** $\hat{\tau} < \hat{\tau}_{max}$ **then**
6: Generate a second uniformly distributed random number, $r_2 \in (0, 1)$, and select the reaction, indexed by μ, such that $\sum_{i=1}^{\mu-1} a_i < a_0 r_2 \leq \sum_{i=1}^{\mu} a_i$ is satisfied.
7: Update the structure of the spring network according to chosen reaction.
8: **end if**
9: Set $\hat{t} = \hat{t} + \min\{\hat{\tau}, \hat{\tau}_{max}\}$. Calculate net forces acting on each point, and update positions by solving $\Sigma \hat{\boldsymbol{F}}_i = \boldsymbol{0}$
10: **end while**

S.1.2 Continuum simulations

In the continuum model (see Section 2.2), we solve a microscale advection–reaction system (Eq. 13) coupled to a second order macroscale PDE (Eq. 20). The macroscale PDE is solved using a finite difference scheme, subject to the boundary conditions in Eq. 23.

We discretise the macroscale domain, $X \in [0, 1]$, into N points with an equal spacing of $\Delta X =$

$1/(N-1)$. Macroscale variables V, H, and B (defined in Eqs. 8, 21) are discretised into the vectors $\boldsymbol{v} = (V_1, V_2, ..., V_N)^T$, $\boldsymbol{h} = (H_1, H_2, ..., H_N)^T$, and $\boldsymbol{b} = (B_1, B_2, ..., B_N)^T$, respectively, where the built-in MATLAB function `trapz` is used in calculating the elements of $\boldsymbol{h}$ and $\boldsymbol{b}$ from microscale distributions (see Eq. 21).

By using a second order central difference in Eq. 20, we solve for $\boldsymbol{v}$ through a matrix equation of the form

$$\boldsymbol{v} = \boldsymbol{A}^{-1}\boldsymbol{p}, \tag{S1}$$

where the vector $\boldsymbol{p}$ is given by

$$\boldsymbol{p} = \left(\alpha\omega\cos(\omega t), \gamma H_2, ..., \gamma H_N\right)^T, \tag{S2}$$

and the matrix $\boldsymbol{A}$ is

$$\boldsymbol{A} = \begin{pmatrix} 1 & 0 & 0 & 0 & 0 & \dots & 0 \\ \frac{1}{\Delta X^2} & D_2 & \frac{1}{\Delta X^2} & 0 & 0 & \dots & 0 \\ 0 & \frac{1}{\Delta X^2} & D_3 & \frac{1}{\Delta X^2} & 0 & \dots & 0 \\ \vdots & \ddots & \ddots & \ddots & \ddots & \ddots & \vdots \\ 0 & \dots & 0 & \frac{1}{\Delta X^2} & D_{N-2} & \frac{1}{\Delta X^2} & 0 \\ 0 & \dots & 0 & 0 & \frac{1}{\Delta X^2} & D_{N-1} & \frac{1}{\Delta X^2} \\ 0 & \dots & 0 & 0 & 0 & \frac{2}{\Delta X^2} & D_N \end{pmatrix}. \tag{S3}$$

The diagonal elements, $D_2, ..., D_N$, are given by $D_i = -\frac{2}{\Delta X^2} - \frac{\gamma}{\delta}B_i$, for $i \in \{2, ..., N\}$, where B_i are elements of the discretised bound fraction vector, $\boldsymbol{b}$, as defined above. Eq. S1 is solved alongside the microscale advection–reaction system (Eq. 13), for which we evolve discretised microscale distributions, $b(x, t; X)$, using the built-in MATLAB function `ode15s` with a first order upwind scheme for the spatial derivatives. We evolve microscale distributions at each of the N (macroscale) discretised points, and distributions are coupled through the solution of $\boldsymbol{v}$.

S.2 Parameter values

S.2.1 Dimensionless parameter values

Dimensionless parameter values used in the continuum and discrete simulations, unless otherwise stated in figure captions, are given below.

Parameter	Description	Value
K_A	Cell Stiffness	2
K_E	ECM Stiffness	4
h	Integrin binding range	1
s	Maximum integrin range	1.5
h_1	Dimensionless unbinding parameter (Eq. 15)	0.5
h_2	Dimensionless unbinding parameter (Eq. 15)	0.4
h_3	Dimensionless unbinding parameter (Eq. 15)	5000
δ	Ratio of microscale binding range, $\hat{h}$, to macroscale lengthscale $\hat{L}$	0.05
ν	Ratio of microscale binding range, $\hat{h}$, to microscale characteristic length, $\hat{l}$.	5
ω	Frequency of oscillatory loading	20

Table S1: Dimensionless parameter values for the continuum simulations, unless otherwise stated in figures.

Parameter	Description	Value
N_{I_A}	Number of I_A nodes	300
N_E	Number of E nodes	500
κ_a	Cell Spring Constant	$2(N_{I_A}\text{-}1)$
κ_r	Restoring Spring Constant	$2(N_{I_A}\text{-}1)$
κ_e	ECM Spring Constant	$4(N_E\text{-}1)$
κ_b	Integrin Spring Constant	1.8
h	Integrin binding range	1
s	Maximum integrin range	1.5
h_1	Dimensionless unbinding parameter (Eq. 15)	0.5
h_2	Dimensionless unbinding parameter (Eq. 15)	0.4
h_3	Dimensionless unbinding parameter (Eq. 15)	5000
δ	Ratio of microscale binding range, $\hat{h}$, to macroscale lengthscale $\hat{L}$	0.05
ω	Frequency of oscillatory loading	20

Table S2: Parameter values for the discrete simulations, unless otherwise stated in figures. Note that the cell and ECM spring constants are scaled by $(N_{I_A}\text{-}1)$ and $(N_E\text{-}1)$, respectively, which are the number of cell and ECM springs that act in series between $X = 0$ and $X = 1$ (see Fig. 2).

S.2.2 Dimensional parameter values

The above dimensionless parameters were obtained, where possible, by using dimensional values from the literature (see below). Some parameters were unknown or widely variable in the literature (denoted by **) and are discussed further below.

Parameter	Description	Range of values	Sources	Chosen value
$\hat{T}$	Breathing cycle duration	$2.7 - 5.8$s	[2]	3.9s
$\hat{\omega}$	Frequency (angular) of oscillatory loading	$1.08 - 2.33\text{s}^{-1}$	From $\hat{\omega} = 2\pi/\hat{T}$	1.6s^{-1}
$\hat{g}_1$	Unstressed unbinding rate	$0.012 - 0.04\text{s}^{-1}$	[3], [4]	0.04s^{-1}
$\hat{g}_2$	Unbinding parameter			0.032s^{-1**}
$\hat{g}_3$	Forced unbinding rate	Instantaneous	Model choice	400s^{-1}
$\hat{f}_1$	Unstressed binding rate	$0.015 - 1.5\text{s}^{-1}$	[4], [5]	0.08s^{-1**}
$\hat{h}$	Integrin binding range	$0 - 28$nm	[6]	20nm
$\hat{s}$	Maximum integrin range before unbinding	28nm+	[6]	30nm
$\hat{\lambda}_b$	Integrin spring constant	$0.15 - 2$pN/nm	[7], [8], [9]	0.15pN/nm
$\hat{\rho}$	Number of integrins per unit length	$0 - 0.2\text{nm}^{-1}$	[10]	0.1nm^{-1**}
$\hat{l}$	Characteristic length			4nm
$\hat{L}$	Characteristic length			400nm

Table S3: Dimensional parameter values used to obtain the dimensionless values in Table S1. Parameters that were unknown or widely variable in the literature are denoted by ** and are discussed further below.

The unstressed binding rate $\hat{f}_1$ varies widely in the literature, as it depends on a number of factors including integrin affinity, integrin density and ligand density. Here we have chosen a rate based on [4, 5]; however, higher values have also been used in the simulations of [9, 11]. The unbinding parameter, $\hat{g}_2$, used in the piecewise linear rates (Eq. 3) does not have an equivalent

in the literature, and was chosen to be of the same order of magnitude as the other reaction rates, $\hat{g}_1$ and $\hat{f}_1$. Some parameter values were estimated from known properties of integrins. The integrin binding ranges, $\hat{h}$ and $\hat{s}$ are estimates based on the length of integrins. An upper bound for $\hat{\rho}$ is estimated based on integrin diameters, which are typically between 5-10nm [10]. This suggests a maximum value of $\hat{\rho} = 0.2\text{nm}^{-1}$; however, the integrin density will vary up to this value depending on the extent of integrin clustering.

The constants $\hat{K}_A$ and $\hat{K}_E$ in Eq. 9 are given values (240pN and 480pN respectively) such that the dimensionless stiffness parameters, K_A and K_E in Eq. 17, are $\mathcal{O}(1)$. We make this choice so that the drag arising from bound integrins, $F(X,t)$, influences the macroscale dynamics via Eq. 17, since integrins are known to be able to influence cell and ECM deformation.

Naturally there is some uncertainty associated with the above parameters, and we have investigated the effect of varying some of these. We find that the qualitative behaviours reported in the main text appear for a range of parameter values, with some examples discussed in Section S.3.1 and shown in Figs. S1 and S2.

S.3 Additional simulations

Using the continuum model, we can also investigate the effect of varying the oscillation frequency, material stiffnesses, and binding affinities (Section S.3.1). We show that these parameters affect the position and width of the bistable region, and demonstrate that the dynamics we observe can be found for a range of parameter values. In Section S.3.2, we will consider the effect of varying the waveform representing tidal breathing since, in reality, this will not be perfectly sinusoidal.

S.3.1 Effect of varying the model parameters

We first consider the effect of varying the oscillation frequency. An increase in the frequency of applied oscillations results in a decrease in the averaged bound integrin density, $\langle B_{tot} \rangle$, on both stable branches (Fig. S1(a)). This is due to reduced contact times for integrin binding. The most significant shift occurs in the lower branch where rupture and rebinding must occur at each cycle; the increased frequency prevents significant binding. The location and size of the bistable window are also affected; for increased frequencies the lower branch persists for lower amplitudes, A, and the bistable region widens. The end points of the high and low branches have been calculated (to the nearest 0.005), giving the widths of the bistable region to be in the ranges $[0.03, 0.04]$, $[0.045, 0.055]$, and $[0.055, 0.065]$ for $\omega = 10$, 20, and 30 respectively.

The material stiffnesses K_A and K_E influence the microscale distributions through the parameter γ that appears in the macroscale relative velocity (Eqs. 20, 21). As seen by Eq. 21, the value of γ decreases when either K_A or K_E are increased; similarly, γ increases when either K_A or K_E are reduced. Without loss of generality, in Fig. S1(b) we present results corresponding to variations in K_A. We observe that an increased cell or ECM stiffness (i.e. reduced γ) leads to a narrowing of the bistable region and a significant downward shift in the amplitude of forcing at which the saddle node bifurcations occur, and where the high branch exists. This is due to increased propagation of the forcing across the macroscale domain resulting from reduced attenuation of the oscillatory load (results not shown). For stiffer cells a lower oscillation amplitude can therefore result in the same degree of bond rupture.

Since binding affinities are specific to integrin type and can vary due to integrin activation and intracellular signalling [12, 13], we also investigate how the magnitude of and transitions between

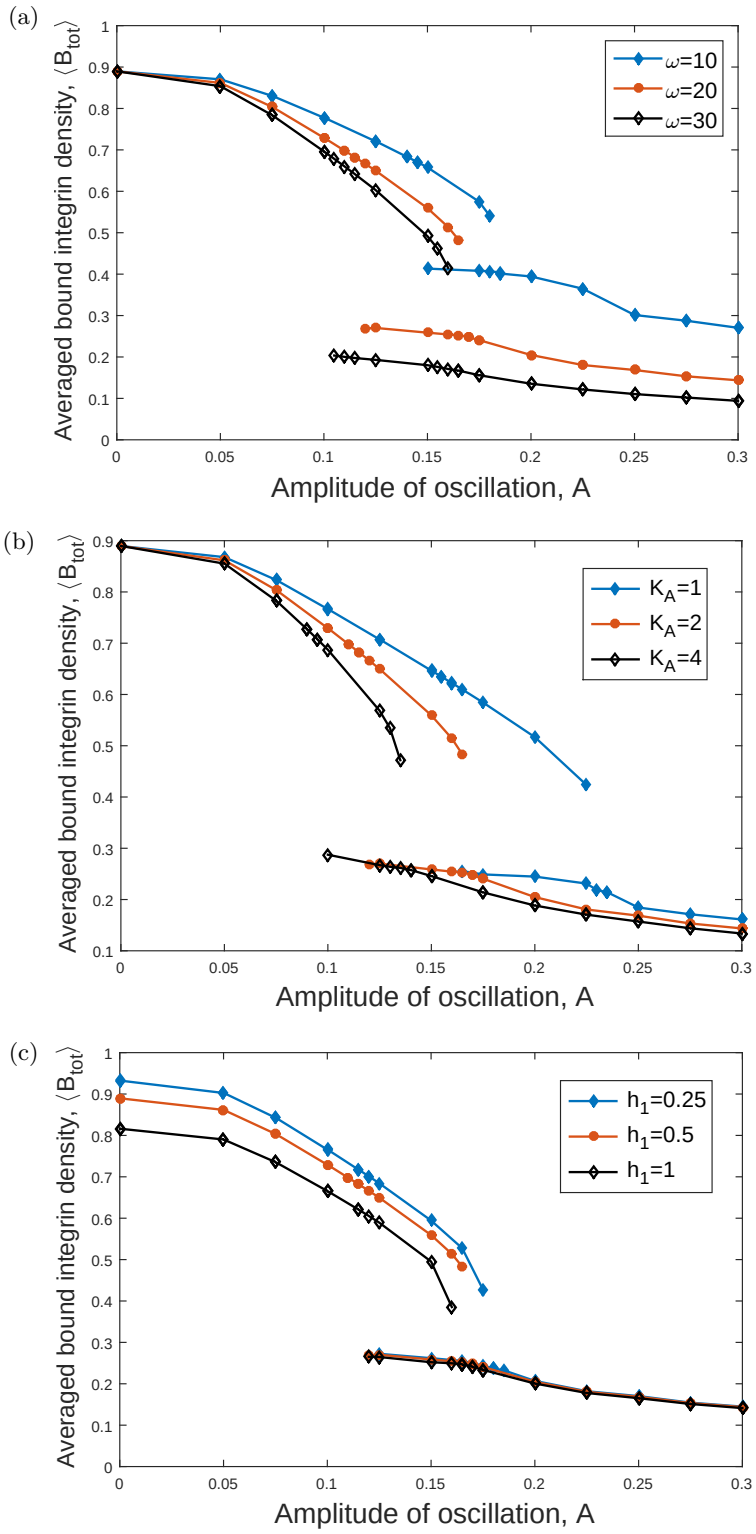

Figure S1: Stable branches in the continuum model (Section 2.2) indicating the values of $\langle B_{tot} \rangle$ (Eqs. 27,28) for: (a) varying frequencies of the oscillatory loading, $\omega = 10$, 20, and 30 (Eq. 18); (b) varying cell stiffnesses, $K_A = 1$, 2, and 4; and (c) varying integrin binding affinities $h_1 = 0.25$, 0.5 and 1 (Eq. 15). For increased frequencies, contact times for integrin binding are reduced, leading to lower averaged bound integrin densities. For increased stiffnesses, there is a significant downward shift in the amplitude of oscillation at which the saddle node bifurcations occur. Binding affinities affect the magnitude of the stable adhesion states, most notably the upper branch, as well as the position and width of the bistable region. Unless otherwise stated, dimensionless parameter values are as in Table S1.

stable adhesion states respond to variations in binding affinities. In Eq. 15 the rupture rates involve parameters h_1, h_2, h_3, the ratios of unbinding rates $\hat{g}_1$, $\hat{g}_2$, $\hat{g}_3$ to the maximum binding rate $\hat{f}_1$ (see Eqs. 2, 3). Here we vary h_1, the unbinding rate for integrins at $x = 0$. We find that the magnitudes of the high stable states decrease with increased h_1 (Fig. S1(c)), since this state is obtained when adhesion formation and rupture balance, i.e. when the system is subject to only small fluctuations. Additionally, the bifurcation point on the top branch shifts to a lower value of A as h_1 increases, as deformation-induced rupture will dominate under lower loading if the bound fraction $\langle B_{tot} \rangle$ is reduced. The shift in stable branches is most notable in the upper branch since the high equilibrium bound state is more sensitive to h_1, the unbinding rate at $x = 0$, than the low oscillatory rupture state. In Fig. S2 we show the effect of varying h_1 with a reduced frequency of oscillatory loading, where the separation in the low branch becomes more apparent since the integrins spend more time in an unstressed state in this regime. The separation is still small since the rates h_2 and h_3, which control the unbinding of integrins in a stressed state (see Eq. 15), are dominant on this branch.

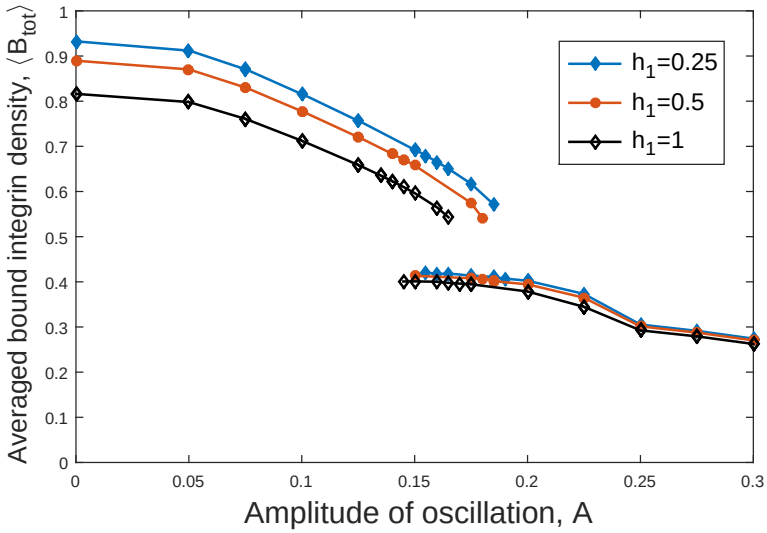

Figure S2: Stable branches indicating the values of $\langle B_{tot} \rangle$ (Eqs. 26,27) as a function of oscillation amplitude, A, for different $h_1 = 0.25$, 0.5 and 1 in Eq. 15 for $\omega = 10$. The lower branches separate (compared to in Fig. S1(c) with $\omega = 20$) due to the lower frequency of oscillations.

S.3.2 Effect of varying the input waveform

Typically, breathing is not perfectly sinusoidal, with a longer time spent on exhalation than inhalation. Here we have considered how an asymmetric waveform (accounting for physiological differences in inhalation and exhalation times) may affect the bound integrins, compared to the sinusoidal waveform used to represent breathing in the main text. We implement the asymmetry by replacing the sinusoidal displacement condition in Eq. 18 by a boundary condition of the form

$$U_E(0,t) = A\sin(\omega t + \alpha\sin(\omega t)), \tag{S4}$$

where A and ω control the amplitude and frequency of oscillation, respectively, and α is a skewness parameter. Note that Eq. 18 and the results in the main text are recovered when $\alpha = 0$. The waveform in Eq. S4 is shown in Fig. S3, where we have chosen to use $\alpha = 0.4$. Denoting the inhalation and exhalation times by t_I and t_E, respectively, this gives $t_I/t_E \approx 0.62$, which is within the range of ratios reported during tidal breathing in [2]. In the sinusoidal case used in the main text (Eq. 18), this ratio was $t_I/t_E = 1$.

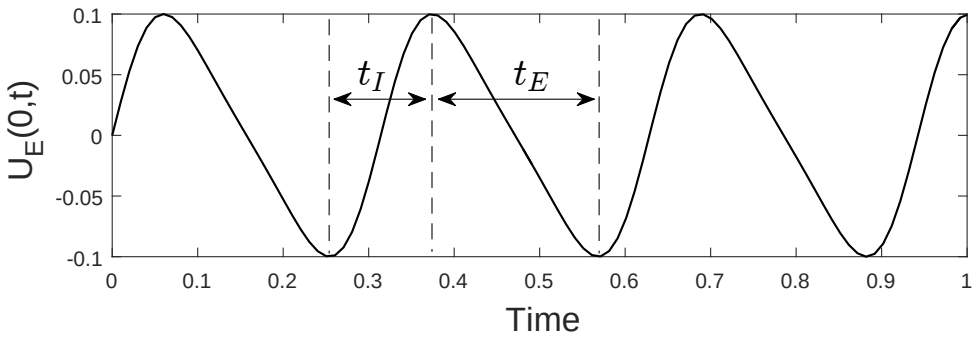

Figure S3: Plot of the asymmetric waveform used for $U_E(0,t)$, given by Eq. S4 with $\alpha = 0.4$, $A = 0.1$ and $\omega = 20$. The times t_I and t_E represent inhalation and exhalation, respectively, and in this case $t_I/t_E \approx 0.62$.

Since the model is driven by the relative velocity at $X = 0$ (see Eq. 23 and Section S.1.2), we differentiate Eq. S4 with respect to time to obtain

$$V(0,t) = A\omega(1 + \alpha\cos(\omega t))(\cos(\omega t + \alpha\sin(\omega t))). \tag{S5}$$

Additionally, we have used the zero displacement condition for the cell, $U_A(0,t) = 0$ (Eq. 18).

Timecourses of the total bound fraction, B_{tot}, (Eq. 27) as the oscillation amplitude, A, varies is shown in Fig. S4. For each amplitude of oscillation we consider a zero (orange) and saturated (blue) initial condition (Eq. 26), as before. Since the oscillations are now asymmetric (Fig. S3), the oscillations in the total bound fraction also exhibit asymmetry; there is more adhesion formation during the longer exhalation period, and the bound fraction therefore reaches a higher peak than during inhalation. As in Fig. 5 in the main text, for low oscillation amplitudes we find that adhesion formation dominates and a high bound integrin state is obtained. For high oscillation amplitudes, adhesion rupture dominates, resulting in a lower bound integrin regime. For intermediate oscillation amplitudes, bistability is again observed due to shared loading between integrins; the outcome depends on the initial condition.

In Fig. S5 we show the stable solution surfaces for a range of amplitudes of oscillatory loading, which corresponds to Fig. 6 in the main text. Since the results are time-averaged over a full cycle, they exhibit only slight differences. The bistable window is slightly wider (a difference of 0.05) in the asymmetric case. As the t_I/t_E value decreases from 1 (corresponding to the symmetric case), the asymmetry in the bound fraction timecourses will become increasingly apparent; however, we expect the results to exhibit the same overall dynamics.

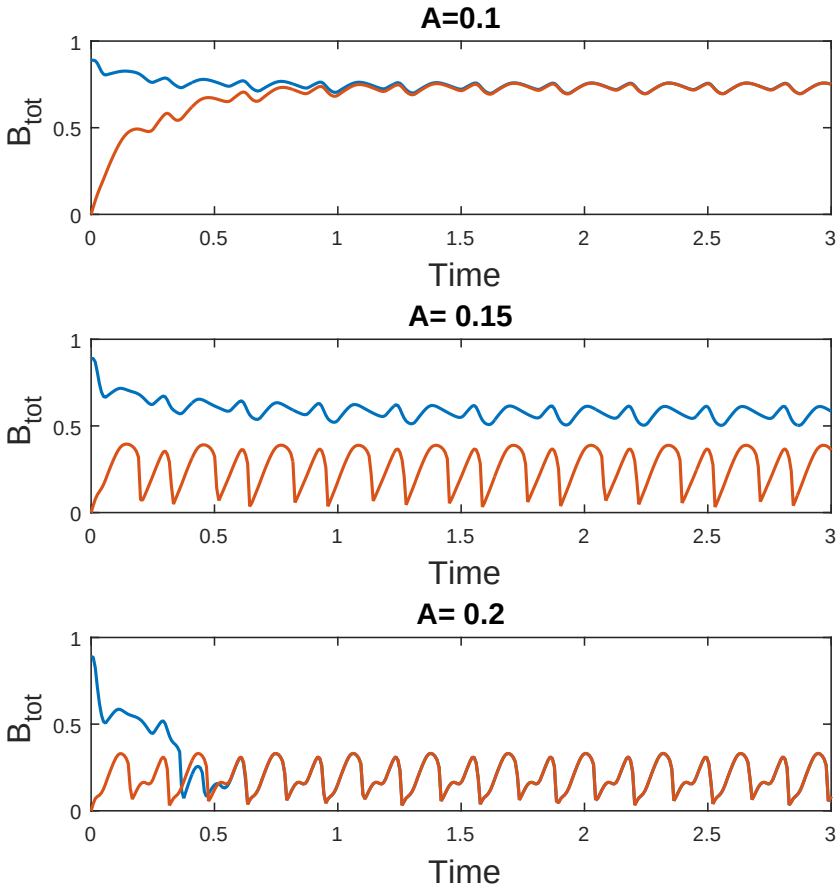

Figure S4: Timecourses illustrating the responses of total bound integrin fractions (Eq. 27) to low ($A = 0.1$), intermediate ($A = 0.15$) and high ($A = 0.2$) amplitude oscillatory loading. This is applied via the boundary conditions in Eq. S5 with $\omega = 20$. In each case we consider a zero (orange) and a saturated (blue) initial condition (Eq. 26).

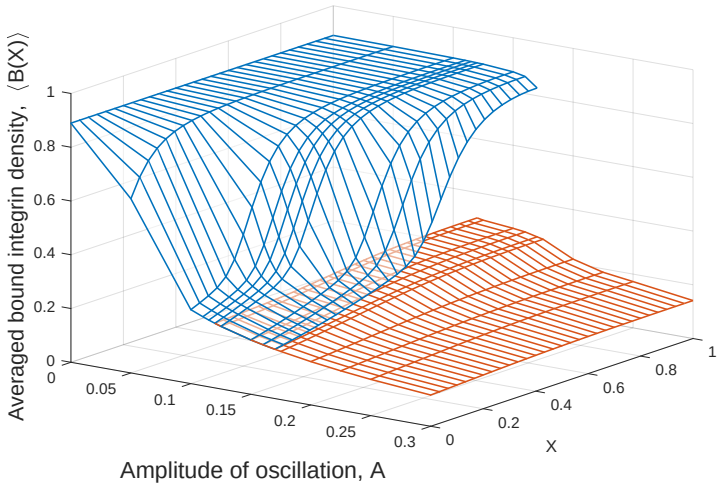

Figure S5: Upper (blue) and lower (orange) stable solution surfaces for the asymmetric waveform in Equation S4. For intermediate values of A there is bistability. The corresponding result with a symmetric waveform is shown in Fig. 6 in the main text.

Supporting References

[1] Gillespie, D. T., 1977. Exact Stochastic Simulation of Coupled Chemical Reactions. *The Journal of Physical Chemistry* 81:2340–2361.

[2] Williams, E. M., T. Powell, M. Eriksen, P. Neill, and R. Colasanti, 2014. A pilot study quantifying the shape of tidal breathing waveforms using centroids in health and COPD. *Journal of clinical monitoring and computing* 28:67–74.

[3] Li, F., S. D. Redick, H. P. Erickson, and V. T. Moy, 2003. Force measurements of the $\alpha 5 \beta 1$ integrin–fibronectin interaction. *Biophysical journal* 84:1252–1262.

[4] Selhuber-Unkel, C., T. Erdmann, M. Lopez-Garcia, H. Kessler, U. S. Schwarz, and J. P. Spatz, 2010. Cell adhesion strength is controlled by intermolecular spacing of adhesion receptors. *Biophysical journal* 98:543–551.

[5] Welf, E. S., U. P. Naik, and B. A. Ogunnaike, 2012. A spatial model for integrin clustering as a result of feedback between integrin activation and integrin binding. *Biophysical Journal* 103:1379–1389.

[6] Nermut, M. V., N. M. Green, P. Eason, S. S. Yamada, and K. M. Yamada, 1988. Electron microscopy and structural model of human fibronectin receptor. *The EMBO journal* 7:4093–4099.

[7] Deshpande, V. S., M. Mrksich, R. M. McMeeking, and A. G. Evans, 2008. A bio-mechanical model for coupling cell contractility with focal adhesion formation. *Journal of the Mechanics and Physics of Solids* 56:1484–1510.

[8] Gao, H., J. Qian, and B. Chen, 2011. Probing mechanical principles of focal contacts in cell-matrix adhesion with a coupled stochastic-elastic modelling framework. *Journal of the Royal Society, Interface / the Royal Society* 8:1217–1232.

[9] Paszek, M. J., D. Boettiger, V. M. Weaver, and D. A. Hammer, 2009. Integrin clustering is driven by mechanical resistance from the glycocalyx and the substrate. *PLoS Computational Biology* 5.

[10] Lepzelter, D., O. Bates, and M. Zaman, 2012. Integrin clustering in two and three dimensions. *Langmuir* 28:5379–5386.

[11] Kong, D., B. Ji, and L. Dai, 2010. Stabilizing to disruptive transition of focal adhesion response to mechanical forces. *Journal of Biomechanics* 43:2524–2529.

[12] Hynes, R. O., 2002. Integrins: bidirectional, allosteric signaling machines. *Cell* 110:673–687.

[13] Hughes, P. E., and M. Pfaff, 1998. Integrin affinity modulation. *Trends in cell biology* 8:359–364.